



# A viscosity study of charcoal-based nanofluids towards enhanced oil recovery

Ifeoluwa Akande<sup>a</sup>, Tony Bridgwater<sup>a</sup>, Petra J. van Koningsbruggen<sup>b</sup>, Qingchun Yuan<sup>a,b,\*</sup>

<sup>a</sup> Energy and Bioproducts Research Institute, College of Engineering and Physical Sciences, Aston University, Birmingham B4 7ET, UK

<sup>b</sup> Department of Chemical Engineering and Applied Chemistry, School of Infrastructure and Sustainable Engineering, Aston University, Birmingham B4 7ET, UK

## ARTICLE INFO

### Keywords:

Charcoal nanoparticles  
Charcoal-based nanofluids  
Viscosity enhancement  
Enhanced oil recovery

## ABSTRACT

Research into nanofluids for enhanced oil recovery (EOR) has been carried out for more than a decade. Metal oxide nanoparticles dispersed in water are usually applied and the nanofluids can recover 8–16 % more of the original oil in place after or comparing to water flooding, while the oil recovery capacity of carbon tube nanofluids can be even better. Higher viscosities of nanofluids than that of water are one of the key properties that contribute to their good performance in EOR. This work, for the first time, prepared nanofluids from two charcoal samples as well as an active carbon sample for their possible application for EOR. The relationship of nanofluid viscosities with pH values as well as nanoparticle concentrations of the nanofluids was studied for their viscous behaviour in different shear conditions. Their representative viscosity data measured at 100 rpm were examined for the values of the so-called Dispersion Factor (DF). The determined DF values for the charcoal-based nanofluids are close to those of metal oxide nanofluids that have much smaller nanoparticle sizes. The highly porous active carbon nanofluid showed strong viscosity enhancement that is comparable to the values reported for nanofluids of carbon nanotubes. Due to their significant viscosity enhancement and carbon sequestration feature, the charcoal-based nanofluids are promising to be used for EOR.

## 1. Introduction

Oil and gas have been the major resource for energy and chemical feedstock and supported the so-called carbon economy in the last century. The massive use of oil and gas as well as coal has resulted in the concentration increase of greenhouse gases (GHG) in the atmosphere and significant global warming [1]. To tackle the global warming, the Paris Agreement [2] set up the goal to limit global warming to well below 2 °C, preferably to 1.5 °C, compared to the pre-industrial level. To achieve this challenging goal, solutions towards decarbonisation, negative emission and zero-carbon have been under development and are quickly becoming competitive across all economic sectors [3] with oil and gas in the centre.

Although the use of oil and gas emits GHGs, the consumption of oil and gas has been continuously increasing, e.g. to  $3.15 \times 10^{10}$  barrels of oil equivalent in 2019 [4]. Oil storage is estimated to last another 50 years at current production and consumption rates [4]. Cost-effective negative emission or zero-carbon solutions are desired for future oil recovery to support rational applications of oil and gas along with sustainable new development to meet people's needs, and to restrict global

warming to mitigate other negative environmental impacts. This research aims to examine the suitability of charcoal-based nanofluids for enhanced oil recovery through carbon utilisation and sequestration as a negative emission solution for oil and gas recovery.

Enhanced oil recovery refers to the third stage oil recovery operation after the first two stages driven by the formation pressure of the oil reservoir and hydraulic pressure that is made up by injected water (water flooding), respectively. At the beginning of the enhanced oil recovery stage, there exists about 60 % or more of the original oil in place (OOIP) in the oil reservoir. This is due to the nature of the complex porous structure of oil reservoir, which results in the formation of viscous fingers of water and oil dispersed in the reservoir and water flooding shortcuts. To overcome the viscous fingers formed in water flooding and recover the dispersed oil, the flooding fluids with different properties such as higher viscosity than water, lower interfacial tension to the oil and better wettability to the reservoir surface have been used to tailor their relative mobility to the oil phase in the reservoir for enhanced oil recovery. The desired change will increase the volumetric spread of the injected flooding fluids for recovering more OOIP.

Nanofluids are colloidal systems of nanoparticles suspended in a base

\* Corresponding author at: Energy and Bioproducts Research Institute, College of Engineering and Physical Sciences, Aston University, Birmingham B4 7ET, UK.  
E-mail address: [q.yuan@aston.ac.uk](mailto:q.yuan@aston.ac.uk) (Q. Yuan).

<https://doi.org/10.1016/j.molliq.2023.122615>

Received 13 March 2023; Received in revised form 9 July 2023; Accepted 17 July 2023

Available online 17 July 2023

0167-7322/© 2023 The Authors. Published by Elsevier B.V. This is an open access article under the CC BY license (<http://creativecommons.org/licenses/by/4.0/>).

fluid, popularly in water. Nanoparticles can provide desirable properties due to their small size and large specific surface area, which situates them to alter the properties, especially the viscosity of the base fluid for enhanced oil recovery. Nanofluids of various metal oxides such as  $\text{SiO}_2$ ,  $\text{Al}_2\text{O}_3$ ,  $\text{TiO}_2$  and  $\text{Fe}_2\text{O}_3$  have been examined for their performance in enhanced oil recovery, and have demonstrated an oil recovery capacity of 8–16 % of the OOIP after water flooding [5–7]. The research described in the literature covers the effect of nanoparticle composition, concentration and other properties such as size/size distribution, shape, porosity and surface chemistry on the viscosity, wettability of the flooding fluid to the reservoir rock and enhanced oil recovery. Youssif et al. [8] studied the oil recovery performance of porous silica nanofluids. The  $\text{SiO}_2$  nanoparticles studied had a monomodal size distribution, averaged at 22 nm, and a specific area of  $370 \text{ m}^2/\text{g}$ . The nanofluids in 3 wt% of NaCl aqueous solution were used to recover the oil loaded in sandstone cores, and the results showed that the oil recovered firstly increase with the silica concentration and reached the maximum oil recovery capacity at a  $\text{SiO}_2$  concentration of 0.1 wt%. At this concentration, a further 13% of the OOIP is recovered after the water flooding or 13% more of the OOIP are recovered comparing to water flooding alone. The  $\text{SiO}_2$  nanofluid of 0.1 wt% was determined to have a viscosity of 1.16 mPas, which is significantly higher than that of water alone.

Along with the physical morphology, nanoparticle surface treatment or formulated with a very small amount of surface active agents or polymers changes the nanoparticle surface chemistry and wettability to the reservoir rock, and the influence of such modifications on  $\text{SiO}_2$  nanoparticle performance has been investigated. Azarshin et al. [9] modified silica nanoparticle (10–15 nm) surface with amine to improve the performance of water flooding in oil wet reservoirs (carbonate cores). Core flood tests of 0.25 wt% of the amine-functionalised silica nanofluid showed a paramount increase of 18% in total oil recovery compared to that of the nanoparticles without surface modification, thus amounting to an impressive 28% increase compared to water flooding alone.

Carbon nanotubes are a group of carbon-based materials that have a hollow cylindrical morphology in the low nanometre range. They are a different type of nanomaterials in terms of the composition and morphology compared to metal oxide nanoparticles and have showed extraordinary capacity in enhancing the viscosity of water [10,11]. It is thus of interest to investigate carbon nanotubes' performance in enhanced oil recovery. Alnarabiji et al. [11] examined the performance of multiwall carbon nanotube (MWCNT) in enhanced oil recovery. Their research showed that the nanofluid of 0.05 wt% MWCNT gave an impressive recovery efficiency of 31.8 % of the residual oil in place.

The focus of our work is on the potential of using charcoals for enhanced oil recovery purposes. Charcoals are derived from biomass (hence relatively cheap and easily accessible from sustainable resources), rich in carbonaceous materials and minerals (metal oxides). A major advantage is that their composition, surface chemistry and porosity can be manipulated by biomass selection, processing condition while producing biofuels. Their origin and manipulatable properties label a possible route to manufacture materials for flooding fluids of oil and gas recovery from sustainable resources, namely biomass. Their variable composition from the biomass type and manufacturing conditions provides a unique possibility for their nanofluids to perform similarly or beyond that of metal oxide nanofluids, while the utilisation of charcoal-based nanofluids also provides opportunities to sequester the carbon in the reservoir. These appeal characteristics have motivated us to carry out our present research into developing charcoal-based nanofluids for enhanced oil recovery. Evidently, preparing charcoal-based nanofluids and examining their viscosity nanofluids is a key step for the development. This paper reports the first piece of work preparing charcoal-based nanofluids and studying their viscosities. Wheat straw and rice husk are massively produced agriculture wastes of food production that are exceedingly investigated for their waste valorisation. Wheat straw, and especially rice husk, is composed of a

significant amount of minerals. Rice husk contains ~ 20 wt% of silica [12,13] and wheat straw contains ~ 7 wt% of silica [14]. These minerals remain as ash in the charcoal after pyrolysis. Wheat straw and rice husk chars, therefore, have been selected in this study as examples. A commercial active carbon has also been examined as reference.

## 2. Experimental section

### 2.1. Materials

The charcoals studied in this work were prepared from wheat straw or rice husk via pyrolysis. The wheat straw char (WSC) was produced using an Auger reactor with a residence time of 10 min at  $400^\circ\text{C}$  [15]. The rice husk char (RHC) was produced using a fixed bed pyrolysis reactor with a residence time of 30 min at  $450^\circ\text{C}$  [16]. A commercial active carbon sample (AC) (Sigma Aldrich, LOT: MKBQ9520V) was used as a reference.

### 2.2. Nanofluid preparation

The charcoal samples prepared by pyrolysis were in the size range of a few millimetres. To reduce the charcoal particles to the desired nanometre size range, an initial grinding using a mortar and pestle was performed to the particle size being less than 40 mesh, followed by wet bead milling in deionised water using a DYNOMILL research Lab or a planetary micro mill Pulverisette 7. Zirconium oxide beads of 0.3 mm and 0.1–0.2 mm were used in stages in the wet bead milling. The wet bead milling was carried out stagewise starting from 5 wt% charcoal. When the fluid became too thick to flow or the particle size reduction not significant, the fluid was diluted using deionised water for further milling until particle sizes were reduced to the desired range. Dynamic Light Scattering (DLS) is applied for examining the particle size and size distribution. Each sample was diluted and adjusted using 0.1 M HCl or NaOH aqueous solution to have a desired pH value and then subjected to ultrasonication for 1 h before the DLS measurement.

### 2.3. Characterisation of charcoals and their nanofluids

#### 2.3.1. Proximate and ultimate analysis

Proximate analysis was carried out using a Mettler Toledo Thermogravimetry Analysis/Differential Scanning Calorimetry apparatus with STAR<sup>e</sup> software for data recording. Sample preparation, the characterisation of the content of moisture and ash follows ASTM standards E1757-19 and E872-82, respectively. The organic matter content is taken as the difference from 100%.

The ultimate analysis was carried out using a CHNS/O Flash 2000 Organic Elemental Analyser (Thermo Fisher Scientific). An accurately weighed sample of 2–3 mg was combusted, and the released gas was analysed for  $\text{CO}_2$ ,  $\text{H}_2\text{O}$ ,  $\text{NO}_2$  and  $\text{SO}_2$  by gas chromatography for the content of C, H and N, respectively. The difference of C, H, N and ash content from 100 % is assigned as oxygen content. The reported data are the average of three measurements with an error of less than 0.3%.

#### 2.3.2. Fourier-Transform Infrared (FTIR) spectroscopy

The FTIR spectra were recorded on a PerkinElmer Frontier FTIR Spectrometer with PEAK Technologies GladiATR sampling accessory. Before measuring the sample, background scans were obtained to reduce the effect of atmospheric  $\text{CO}_2$  and moisture on the spectral background. The measurement comprised of 16 scans carried out in the range of  $4000$  to  $400 \text{ cm}^{-1}$  at a resolution of  $4 \text{ cm}^{-1}$ .

#### 2.3.3. pH at the point of zero charge (PZC)

To characterise the charcoal surface charging condition, the pH point of zero charge ( $\text{PZC}_{\text{pH}}$ ) was determined for each sample. The  $\text{PZC}_{\text{pH}}$  of a material is the pH value at which the material surface is neutral, thus having a zero charge. A solid addition method adapted from [17] was

used to determine the point of zero charge of the charcoal samples. NaOH (0.1 M) and HCl (0.1 M) aqueous solutions were used to prepare six starting solutions of 12 mL, each having an initial pH value of 1, 3, 5, 7, 9 or 11, respectively. Charcoal samples of 0.1 g were dispersed into each solution. The mixtures were stirred in a water bath of 25 °C for 24 hrs. The pH value of each mixture was then recorded as the final pH value. The final pH values were plotted against the initial ones to determine the point of zero charge, which is the pH where the initial and final pH are equalised. All the measurements were repeated three times. A Jenway 3540 pH and conductivity meter was used in the pH measurement. The pH meter was calibrated using buffer solutions of pH 4.0, 7.0 and 9.2 on a daily basis before the measurement.

### 2.3.4. Particle size and zeta potential measurement

The charcoal particle size and size distribution in the milled fluid were analysed using a Brookhaven Zeta plus. To avoid any agglomeration and measure the primary size of the charcoal particles, the milled fluids were extensively diluted and ultrasonicated after adjusting pH away from their PZC<sub>pH</sub>. Each sample was repeated at least three times and averages of repetitive measurements were reported.

### 2.3.5. Optical and electronic microscopic imaging

A Motic BA310 Digital Biological Microscope with an objective lens of 4×, 10×, 40 × and 100 × was used for the examination of charcoal-based fluids at varied pH values. A drop of the diluted fluid at a controlled pH value was placed on a glass slide. Gently shake the slide to form a thin layer of sample film for observation. The scale bar was calibrated using the microbar provided by Motic.

An Environmental Scanning Electron Microscope (Thermo Quattro S) was used to observe the charcoal nanoparticles. A nanofluid sample prepared was extensively diluted and a drop of the diluted sample was carefully placed on a copper grit for evaporation overnight and then loaded for observation.

### 2.3.6. Viscosity measurement of nanofluids

The viscosity was measured using a Brookfield DV-II Ultra cone or plate (CPA-42) rheometer. The viscosity measurement was carried out either at a given shear rate of 384 s<sup>-1</sup> (100 rpm) or in the shear rate ranging from 10 to 200 s<sup>-1</sup> at a given temperature, which was controlled by a Thermo Haake C25P bath with an accuracy of ± 0.1 °C. The rheometer was calibrated by the viscosity of water at 25 °C. Each fluid sample was ultra-sonicated for 1 hr at 25 °C directly before the measurement. Each sample was measured at least three times ensuring that the reported data had an accuracy within ± 0.1 mPa.s.

## 3. Results and discussion

### 3.1. Characterisation of the charcoal samples

The selected wheat straw char (WSC), rice husk char (RHC) and active carbon (AC) were first analyzed for their proximate and ultimate compositions, as shown in Table 1.

The three samples are all rich in ash, of which the RHC contains the highest amount at 33.56 wt%, WSC at 11.16 wt% and AC at 9.56 wt% on

**Table 1**  
Proximate and ultimate analyses of the charcoals studied.

	WSC	RHC	AC
Proximate Analysis (wt. %, dry basis)			
Ash	11.16	33.56	9.56
Organic Matter	88.84	66.44	90.44
Ultimate Analysis (wt.%, dry basis)			
C	74.33	52.63	55.89
H	3.91	3.40	2.68
N	1.01	0.79	0.45
O (by difference)	9.59	9.62	31.42

dry basis. Rice husk itself contains ~ 20 wt% of silica [12,13] and wheat straw contains ~ 7 wt% of silica [14] and ~ 1.2 wt% of K, Mg and Ca, of which potassium is most dominant at ~ 1 wt% [18]. Carbon is the richest element as organic matter, which is, on dry basis, 74.33 wt% for WSC, 52.63 wt% for RHC and 55.89 wt% for AC. The AC contains 31.42 wt% oxygen on dry basis, while the oxygen contents for WSC and RHC are close at 9.59 wt% and 9.62 wt%, respectively.

The charcoals, as well as AC, are analysed by FTIR spectroscopy. Their IR spectra are displayed in Fig. 1. The IR spectra of RHC and WSC have strong absorption bands at 795 and 1080 cm<sup>-1</sup>, which can be assigned to the stretching and bending vibrations of Si-O [19–21], respectively. This is consistent with the fact that RHC and WSC are rich in silica [12–14]. The vibrational bands of silica cannot be found in the IR spectrum of AC, suggesting that little silica is present in the AC.

The IR spectra of the three samples all have a wide band at ~ 3350 cm<sup>-1</sup>, and significant bands in the range of ~ 1600–1575 cm<sup>-1</sup> and 1500–1400 cm<sup>-1</sup>, which can be assigned to the O–H vibrations of carboxylic or phenolic groups, and skeletal C–C stretch vibration in aromatic rings, respectively. These bands are stronger in the WSC and AC IR spectra than in the RHC IR spectrum, reflecting the higher carbon-based organic content in WSC and AC compared to RHC. The IR spectrum of WSC, as well as that of AC, shows absorption bands at 1319 cm<sup>-1</sup> assigned to C–O stretching vibrations, and at 875 cm<sup>-1</sup> assigned to C = C bending vibrations. In addition, the AC IR spectrum shows absorption bands in the IR fingerprint zone at 1171 cm<sup>-1</sup>, 988 cm<sup>-1</sup> (C = C bending), 870 cm<sup>-1</sup>, 751 cm<sup>-1</sup> (C–H bending) and 495 cm<sup>-1</sup>. The presence of these various aromatic carbon and oxygen-containing functional groups in conjunction with the elemental composition and ash components being different for all three samples is of importance for the present study as these factors are thought to be responsible for the perceived differences in surface chemistry interactions to the base liquid in the fluid.

The pH point of zero charge (PZC<sub>pH</sub>) was determined for each sample for its surface charging condition in water by the method described above. Fig. 2 shows the final pH values of each sample as function of the various initial pH values.

The data for WSC and RHC show similarly shaped curves with PZC<sub>pH</sub> values located at pH7.4 for WSC and pH6.6 for RHC, implying that the surface charge switches from positive to negative at these respective pH values. The WSC surface shows a slightly alkaline characteristic, which can be attributed to its richness in potassium-containing compounds as evidenced by >1 wt% of potassium in raw wheat straw [18]. This PZC<sub>pH</sub> of pH7.4 determined for WSC is very close to the PZC<sub>pH</sub> value of pH7.8 for another wheat straw char studied by Liu et. al. [17]. The RHC surface is slightly acidic with a PZC<sub>pH</sub> value of 6.6. This PZC<sub>pH</sub> value should be related to the high ash content of RHC at 33.56 wt% (on a dry sample

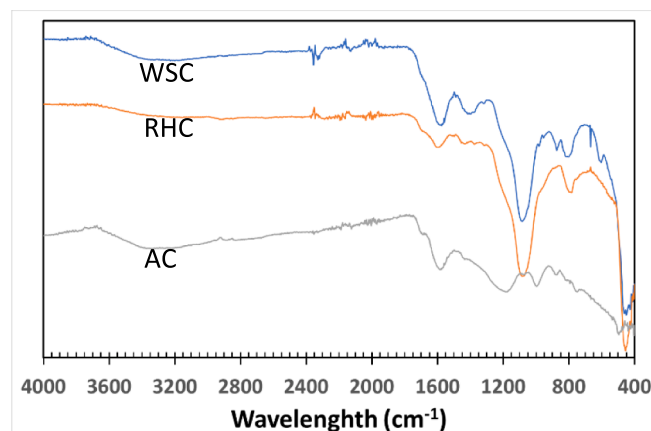


**Fig. 1.** IR spectra of the charcoals studied: WSC = wheat straw char, RHC = rice husk char AC = active carbon.

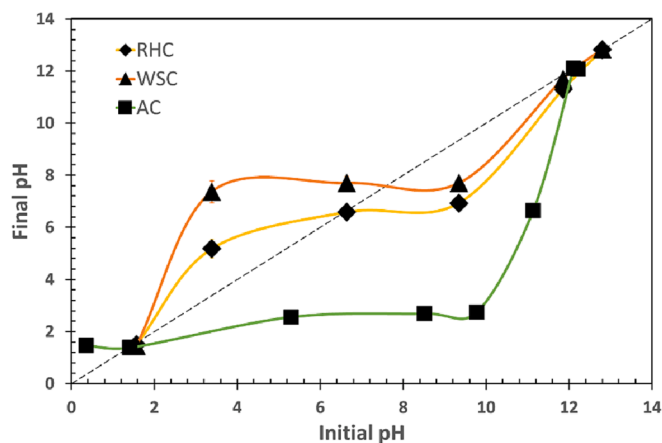


**Fig. 2.** The final pH value versus corresponding initial pH values for aqueous solutions containing RHC, WSC or AC. The dotted line represents  $y = x$  for finding an accurate  $PZC_{pH}$  value.

basis), which is dominated by silica. Both charcoals show a significant surface buffer effect in the range of pH4.0 – 9.2, which is evidenced by the final pH value being levelled in this range (Fig. 2). Subsequently, the final pH gradually increases from pH 9.2 to pH 12.0.

On the other hand, the AC surface is strongly acidic with its  $PZC_{pH}$  at pH1.4. After this  $PZC_{pH}$  value a two-stage surface buffer effect shows in the range of ~ pH2.0–5.0 and ~ pH5.0 to 9.5, and then the final pH value starts to increase considerably, gradually reaching pH12.0. The  $PZC_{pH}$  values are summarised in Table 2, together with the ash content and BET measurement data of specific surface areas and micropore volumes that are determined by  $N_2$  gas adsorption.

Both WSC and RHC have small specific surface areas at 11 and 22  $m^2/g$ , respectively, which is rather small compared to that of AC at 1600  $m^2/g$ . The small specific surface areas of WSC and RHC correspond to their low specific micropore volumes, e.g. 0.027  $cm^3/g$  for the WSC and negligible for RHC. In contrast, the large specific surface area of 1600  $m^2/g$  of AC is associated with a micropore volume of 2.000  $cm^3/g$ , which is the volume of pores with an opening smaller than 2 nm. Compared to the commercially widely used highly microporous AC, the specific surface area and micropore volume are very small for WSC and RHC. The difference allows the study of the effect of a variation in porosity of the nanoparticles on the viscosity of the nanofluid.

### 3.2. Nanofluid preparation and characterisation

The nanofluids prepared by wet bead milling were imaged by both optical and electronic microscopes. The images in Fig. 3 show that when the nanofluids are dried for electronic microscopic imaging, the charcoal nanoparticles are agglomerated together as dried flocs, small or large depending on the sample and their preparation. Under the optical microscope, the agglomeration of charcoal nanoparticles has been observed as re-dispersible by adjusting the pH value of the nanofluids. At an alkaline condition, small particles, smaller than 1  $\mu m$  dispersed in water have been observed for the three nanofluids, which approaches the limit of optical microscopes.

The particle size and size distributions are then measured by DLS at pH 2, 7 and 11 for each of the nanofluid and the results are shown in

**Table 2**  
 $PZC_{pH}$  and specific surface area and micropore volume of the charcoals studied.

Sample	$PZC_{pH}$	BET Surface Area ( $m^2/g$ )	Micropore Volume ( $cm^3/g$ )
WSC	7.4	11	0.027
RHC	6.6	22	< 0.001
AC	1.4	1600	2.000

Fig. 4. The particle size distribution curves are normalised as 100 at particle distribution peaks (the most frequently occurred particle size) to facilitate comparison of the data collected for each nanofluid. The data show that using our methodology, the charcoal particles reduced to the nanosized range have monomodal size distributions, centred around a distinct particle size distribution peak. The detected particle distribution peak size and half peak width of the particle size distribution peak are tabulated in Table 3. Both the peak size and half peak width vary with the pH values, and the pattern is different for each charcoal sample.

For the WSC nanofluid, the centre of the particle size distribution peak is detected at 1292 nm, 96 nm and 92 nm for pH2, pH7 and pH11, respectively. Interestingly, the detected WSC nanoparticles are distinctively large and widely distributed at pH2, which is indicated by both the peak size and half peak width being more than ten times that detected at pH7 and pH11. While the pH value increases from pH7 to pH11, the determined particle size distribution remains about identical, both in size and size distribution. For the RHC nanofluid, the centre of the particle size distribution peak is detected at 408 nm, 154 nm, and 168 nm for pH2, pH7 and pH11, respectively. Also, for the RHC nanofluid, the detected particles appear to be more than doubled in size at pH2 compared to their appearance at pH7 and pH11. While the pH value increases from pH7 to pH11, the centre of the particle size distribution peak is close at 154 nm and 168 nm with a half-width of the particle distribution peak of 80 nm and 87 nm, respectively. For the AC nanofluid, the centre of the particle size distribution peak is detected at 256 nm, 210 nm, and 254 nm at pH2, pH7 and pH11, respectively. Hence, the particle sizes are close to one another, albeit the half peak width decreases from 362 nm, 154 nm to 143 nm when going from pH2 to pH7 to pH11, respectively. The curves in Fig. 5 summarise the variation of the centre of the particle size distribution peak and half peak width with pH values.

The above size measurement study at different pH values shows that the large particle sizes detected at pH2 are obviously nanoparticle clusters rather than individual nanoparticles for WSC and RHC nanofluids even just after the sample for the measurement has been ultrasonicated for one hour. The AC nanofluid at pH2 does include the nanoparticles in a similarly low size range as in the AC samples at pH7 and pH11, but at pH2 the detected particle size distribution is more than twice as wide as that of the samples at pH7 and pH11. These observations align well with the fact that the  $PZC_{pH}$  values of WSC (pH7.4) and RHC (pH6.6) are higher than pH2, which is a pH value that is distinctively away from their surface neutralisation buffer pH range, while the pH2 is somewhat higher than the  $PZC_{pH}$  of AC (pH1.4), which is starting to enter the surface neutralisation buffer pH range. Therefore, the detected nanoparticle size difference between pH2 and pH7 is much larger for WSC and RHC and is relatively small for AC nanofluids.

These nanoparticle size variations with pH values can be related further to their zeta-potential values, which are also shown in Table 3. The zeta-potential indicates the charging intensity of the hydrated layer of nanoparticle surface in the fluid. The data in Table 3 shows that at pH2, the nanoparticles have positive zeta-potentials of 66 mV for the WSC nanofluid, 31 mV for the RHC nanofluid and 9 mV for the AC nanofluid. Upon the pH increase to pH7, their zeta-potentials become negative, with values of -115 mV for the WSC nanofluid, -110 mV for the RHC nanofluid and -21 mV for AC nanofluid. At pH11, the zeta-potentials decrease to -98 mV for the WSC nanofluid and -34 mV for the RHC nanofluid at pH11 and increase further to -30 mV for the AC nanofluid. The zeta-potential variation trends with the pH value are consistent with that of the particle size detected by DLS: the higher the absolute zeta potential value of the hydrated nanoparticles, the smaller the particle size and the narrower the particle size distribution that are detected by the laser beam, suggesting that the nanoparticles separate better when the absolute value of the zeta potential is high, which means that the electrostatic repulsion is high and so the particles effectively repel one another thus promoting particle separation.

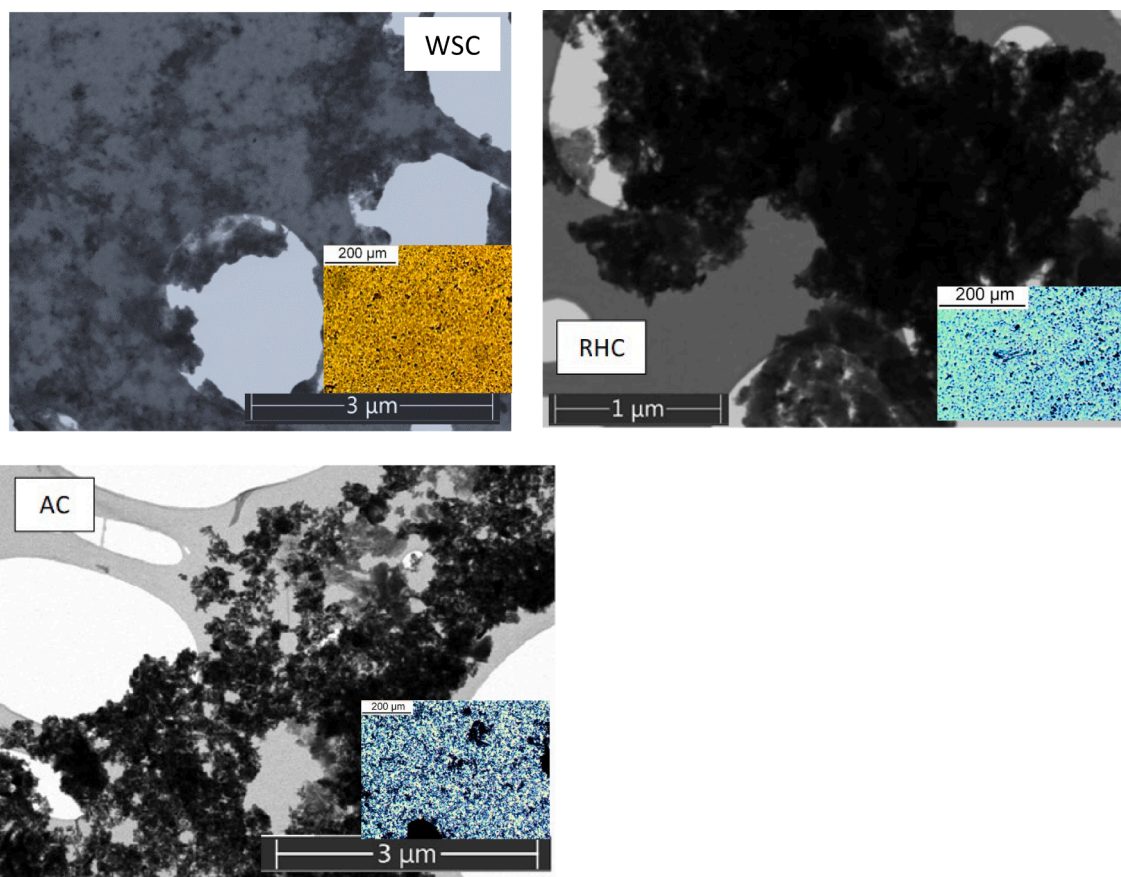


Fig. 3. Electronic and optical microscopic images of the nanofluids prepared from WSC, RHC or AC, respectively. The optical microscopic images are the inset.

### 3.3. Viscosity enhancement of charcoal-based fluids

#### 3.3.1. Effect of pH value on the viscosity

At the first, the effect of pH value on the viscosity is studied for the viscosity enhancement of the charcoal-based fluids. Their viscosity changes with pH values are shown in Fig. 6. The nanoparticle concentrations, which are 1.25 wt% for the WSC, 0.50 wt% for the RHC and 0.63 wt% for the AC nanofluids, were randomly chosen just to demonstrate the viscosity value variation trend with pH values.

Different trends are observed for the variation of the viscosities of the three nanofluids as a function of pH. For the WSC fluid (1.25 wt%), the highest viscosity value has been found at pH2, which is 3.72 mPa·s. The viscosity significantly decreases to 1.16 mPa·s with a pH value increase to pH6, and then its value slightly further decreases to 1.03 mPa·s at pH12 (Fig. 6). The viscosity decreases in tandem with the particle size distribution detected by DLS at different pH values, e.g. the centre of the particle size distribution peak being 1292 nm at pH2, 96 nm at pH7 and 92 nm at pH11. The RHC nanofluid (0.5 wt%) appears to show a small variation in viscosity from 1.09 mPa·s at pH2, 0.96 mPa·s at pH6.8 to 1.02 mPa·s at pH12. This slight viscosity variation follows the detected particle sizes as well, i.e. 408 nm at pH2, 154 nm at pH7 and 168 nm at pH11.

For the interpretation of the recorded data, it is worth considering that it is well known that DLS detects moving particles by their scattering of the laser beam. A particle in contact with other particles is measured as one large particle. In a general sense for one given sample, the larger size of the detected particles can be indicative of stronger interactions between the nanoparticles. For the WSC and RHC fluids, the particle sizes detected at pH2 are several times larger than these at pH7 and pH11 (Fig. 6), suggesting that the larger particle sizes and wider particle size distribution detected by DLS for the same sample at

different pH value conditions, is related to stronger interactions between the nanoparticles. This judgment agrees with the absolute value variation of the zeta-potential. Both these features observed in the DLS measurements for the WSC and RHC nanofluids indicate that a stronger interaction between nanoparticles lead to a higher viscosity increment.

The viscosity of the AC nanofluid (0.63 wt%) increases nearly linearly from 1.8 mPa·s at pH2.0 to 5.2 mPa·s at pH12, while DLS measurements detected similar particle sizes but increasingly narrower size distributions (see Fig. 4c) with increasing pH, suggesting increasingly weakening of interactions between the nanoparticles. In this context, it is worth noting that the different behaviour of AC is related to it being distinctly different from WSC and RHC for its very large specific surface area of 1600 m<sup>2</sup>/g and micropore volume of 2 cm<sup>3</sup>/g. The large specific surface area is resulted from the richness in micropores, which is less than 2 nm. The micropores are in the size range comparable to the empty channels of carbon nanotubes for the study of pore effects.

#### 3.3.2. The effect of nanoparticle type and content on the viscosity of nanofluids

The three nanofluids of WSC, RHC and AC were examined for the effect of particle concentration on viscosity at pH7. The viscosity measurement was carried out at continuously varied shear rates from 10 to 400 s<sup>-1</sup>. The effect of shear rate on the viscosity of each nanofluid at different concentrations is depicted in Fig. 7.

The experimental data in Fig. 7 show that at the concentrations examined all three nanofluids show viscosity enhancement compared to that of the base liquid, deionised water, at the same temperature. Their viscosities show the highest value at the starting shear rate of 10 s<sup>-1</sup> and then decrease with the shear rate to 100 ~ 150 s<sup>-1</sup>, depending on the nanoparticle concentration. After this shear-thinning range at low shear rate, the viscosity of the nanofluids then tends to be levelled.

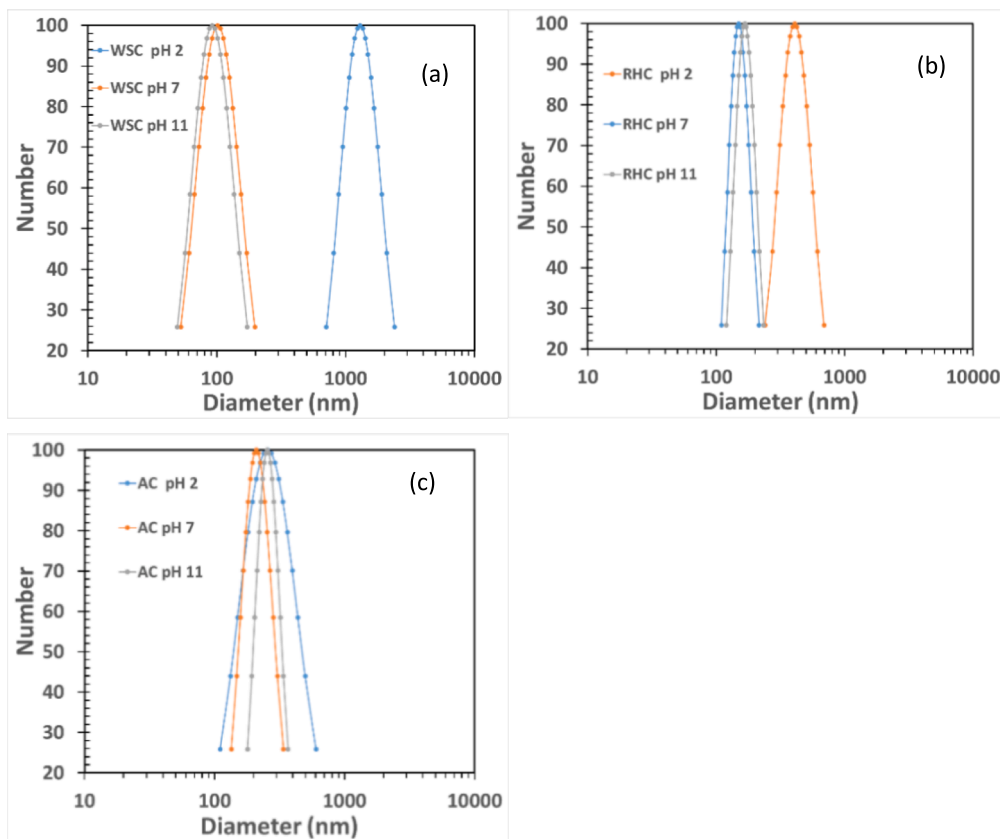


Fig. 4. Effect of pH values on the normalised particle number size distribution of a) WSC, b) RHC and c) AC determined by Dynamic Light Scattering (DLS).

Table 3

The particle distribution peak size (Peak), half peak width (HPW) and  $\zeta$ -potentials of the charcoal-based nanofluids.

Sample	pH2			pH7			pH11		
	Peak, nm	HPW, nm	$\zeta$ -potential, mV	Peak, nm	HPW, nm	$\zeta$ -potential, mV	Peak, nm	HPW, nm	$\zeta$ -potential, mV
WSC	1292	1271	66	96	108	-115	92	92	-98
RHC	408	336	31	154	80	-110	168	87	-34
AC	256	362	9	210	154	-21	254	143	-30

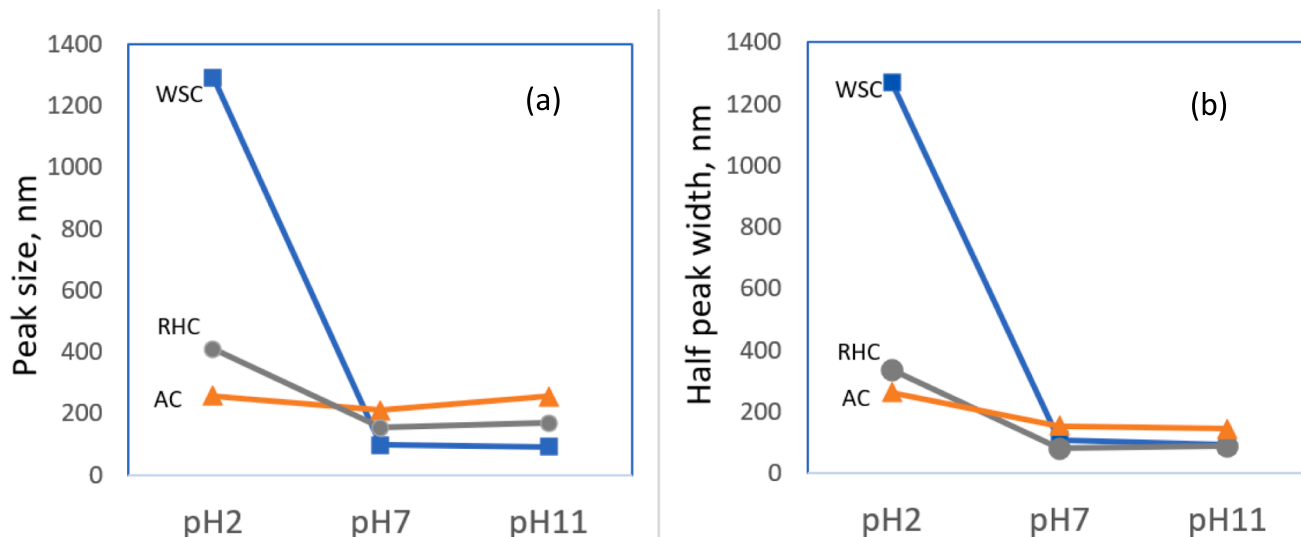


Fig. 5. The centre of the particle size distribution peak (a) and half peak width (b) at selected pH values determined by Dynamic Light Scattering (DLS).

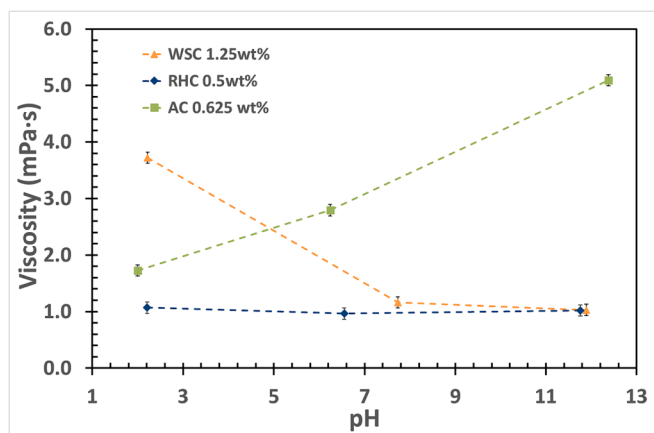


Fig. 6. The effect of pH values of the nanofluids on their viscosities. The viscosity was measured at 100 rpm and 22 °C.

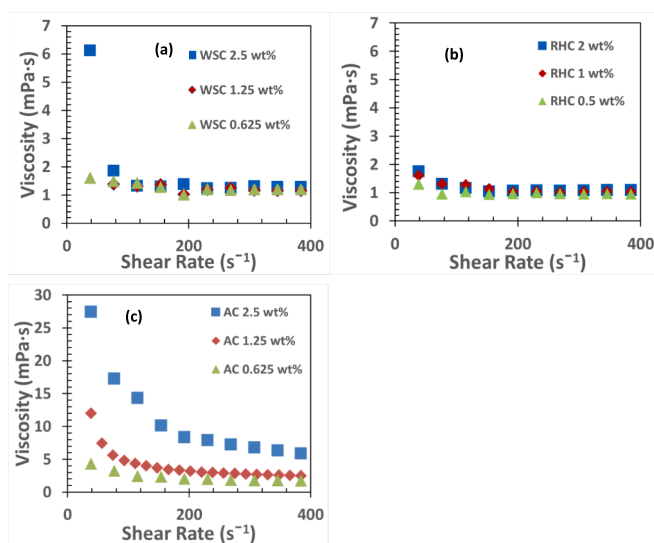


Fig. 7. The effect of shear rates and nanoparticle concentrations on the viscosity of nanofluids: a) WSC, b) RHC and c) AC. The viscosity measurements were carried out at pH6 and a temperature of 22 °C.

The viscosity enhancement increases with the nanoparticle content, but the viscosity increment varies with the particular charcoals in the order: AC > WSC > RHC. At 100 rpm (shear rate 384 s<sup>-1</sup>), a condition that is commonly used to represent the viscosity of fluids, the viscosities

are 2.62 mPa·s for the 1.25 wt% AC and 1.22 mPa·s for the 1.25 wt% WSC, which are 2.94 and 1.37 times that of water, respectively, and the viscosity for the 1.0 wt% RHC nanofluid 1.04 mPa·s, which is 1.17 times of that of water.

The viscosity of the three charcoal-based nanofluids was measured at 100 rpm (shear rate 384 s<sup>-1</sup>) at pH6 and 22 °C for the relationship study of the relative viscosities, the ratio of the effective dynamic viscosity of the nanofluid ( $\eta_{eff}$ ) and the dynamic viscosity of the base liquid ( $\eta_{bf}$ ), to the nanoparticle volume fraction, as shown in Fig. 8a. In the figure, the calculated lines of our equation, Equation (1) [22], modified from Chen’s equation [23], are also included with the best agreement for the Dispersion Factor (DF) being DF = 7.0 for the WSC nanofluids, and DF = 4.5 for the RHC nanofluids.

$$\frac{\eta_{eff}}{\eta_{bf}} = \left(1 - \frac{\phi}{0.605}(DF)^{1.2}\right)^{-1.5125} \quad (1)$$

The calculation used the assumption that the nanoparticles were spherical, and the  $\phi$  is the nanoparticle volume fraction. The modelling shows a least mean square error of 0.066 for the WSC nanofluids and 0.011 for the RHC nanofluids, which are much smaller than the relative viscosity values of the nanofluids that are larger than 1. It is worth noting that the WSC nanoparticles (92 nm at pH7) having DF = 7.0 provide better viscosity enhancement than the best viscosity enhancement achieved by metal oxides with DF = 6.6 for silica nanofluids (20 nm) and DF = 6.2 for alumina nanofluids (45 nm) [22]. The RHC nanofluids (154 nm at pH7) having DF = 4.5 shows a medium viscosity enhancement of metal oxides, comparable to that of the nanofluid of 200–300 nm alumina nanoparticles [22].

The relative viscosity data analysis of the WSC and RHC nanofluids using our modified Chen equation suggests that the nanoparticle size determines the number of interactions between particle and particle as well as between particle and the base liquid, with the nanoparticle surface chemical composition determines strength of these interactions. It must be emphasised that the combined effect of the interaction number and strength is reflected in the relative viscosity and further in the modelled DF value. The DF is thus an extremely useful and valuable parameter for characterising the effectiveness of the viscosity enhancement that is achieved by using a particular nanofluid. The higher the DF value, the more significant the viscosity increment appears at a given nanofluid concentration.

The relative viscosities of the AC nanofluids varying with the nanoparticle volume fraction is shown in Fig. 8b. Instead of following the modified Chen equation, the relative viscosity shows an excellent linear relationship to the volume fraction of the AC nanoparticles as shown by Equation (2) that is obtained by linear regression of the data.

$$\frac{\eta_{eff}}{\eta_{bf}} = 1 + 413.97\phi, R^2 = 0.9904 \quad (2)$$

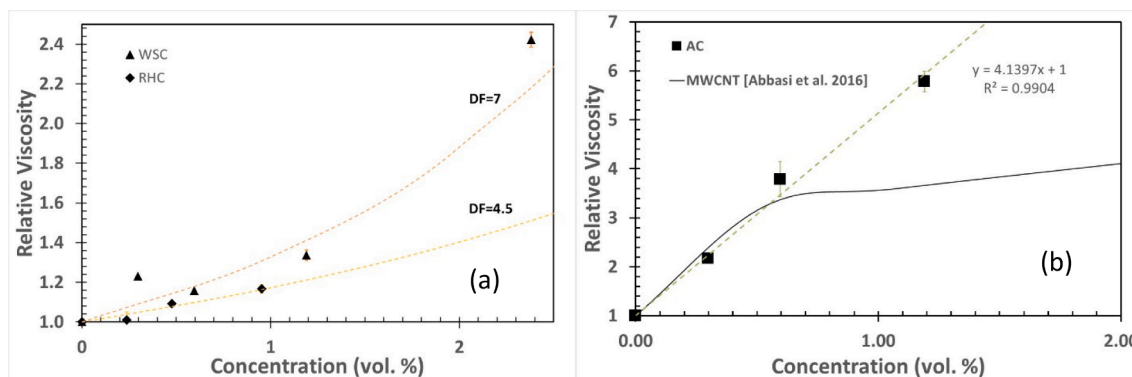


Fig. 8. Relative viscosity of nanofluids versus nanoparticle volumetric fraction: (a) experimental data of the WSC and RHC nanofluids compared to the calculated values using the modified Chen equation (the dotted lines) and (b) the AC nanofluids (the solid square with the regression line) compared to that of carbon nanotube nanofluids (the solid black line). The viscosity was measured at pH6, 100 rpm and 22°C.

where  $\eta_{\text{eff}}$  is the effective dynamic viscosity of the suspension (mPa·s);  $\eta_{\text{bf}}$  is the base liquid dynamic viscosity (mPa·s) at the same temperature; and  $\varphi$  is the volume fraction of the hard spherical particles suspended in the fluid.

Significantly, by Comparing Equation (2) to the Park and Cho expression [24], the viscosity increment of the AC nanoparticles is approximately 10 times higher than that of alumina and titanium oxide nanoparticles.

Among the three nanofluids, the AC nanofluid shows the largest particle size (particle distribution peak size at 210 nm compared to 96 nm for WSC and 154 nm for RHC nanofluids at pH7) and exhibits the most significant viscosity enhancement. This outstandingly high viscosity enhancement of the AC nanofluid can be related to both its richness in oxygen content and polar/hydrophilic functional groups, as shown by the ultimate and FTIR analysis, and more apparently in micropores that are in the range of the hollow structure of carbon nanotubes (~2 nm). Similar to active carbon, carbon nanotubes dispersed in water normally have a hydrophilic surface [25].

To afford further analysis, the viscosity increment of the AC nanoparticles is compared to that of multiwall carbon nanotube (MWCNT) nanofluids in Fig. 8b, showing very much identical viscosity enhancement for both AC and MWCNT when the volume content of MWCNTs is below 0.6 vol% [26], which is much higher than that usually achieved with metal oxide (e.g.  $\text{TiO}_2$ ,  $\gamma\text{-Al}_2\text{O}_3$  and  $\text{SiO}_2$ ) nanoparticles [22]. However, Youssif et. al. [8] found rather high viscosities for some silica nanofluids. They studied viscosity of nanofluids of porous silica nanoparticles (22 nm with a specific area of 370  $\text{m}^2/\text{g}$ ). The nanofluids of 0.01, 0.05, 0.1 or 0.5 wt% in the brine of 3 wt% of NaCl showed viscosities of 1.009, 1.067, 1.160 and 1.347 mPas, respectively. These viscosities are significantly higher than that reported for other silica nanofluids reported by Tavman et. al. [27]. The outstanding viscosity enhancement is believed to have resulted from a so-called pore-effect; this is another indication of the importance of porosity of the nanoparticles constituting the nanofluid in generating high relative viscosity values.

Returning to Fig. 8b, it is important to underline that when the nanoparticle volume content is higher than 0.6 vol%, the MWCNT fluids do not show significant further relative viscosity increase while the AC fluids show a proportional further viscosity increase following Equation (2). An analysis of these various experimental results suggests that the highly porous structure of both the MWCNT and AC nanoparticles and their nanoparticles' free movement in the fluid are critical for the generation of the observed significant viscosity enhancement. The AC nanoparticles are nanosized in three dimensions (3D nanomaterial) while MWCNT is considered to be a 2D nanomaterial for the carbon nanotube's length can be a few magnitudes larger than its diameter of ~2 nm. The high aspect ratio of MWCNT facilitates entanglement of individual MWCNT entities which would limit further viscosity enhancement at a MWCNT concentration higher than 0.6 vol%. At a higher concentration, the 3D nanosized AC particles can move more freely in the nanofluid than is possible for equally concentrated MWCNT in the nanofluids, so that AC's viscosity increment continues to occur when the AC concentration is over 0.6 vol%. The consequence is that nanofluids of the highly porous AC nanoparticles show a similar viscosity increment to MWCNTs due to their similarly high porosity when the content is less than 0.6 vol%. However, the situation changes in favour of AC at a higher concentration as the 3D nanosized AC particles can move more freely in the nanofluid than is possible for MWCNT, so that AC's viscosity increment continues to go on up to a much higher concentration, which reaches up to 1.2 vol% as shown in Fig. 8b, the highest volume fraction measured in this study. The reason and origin of the upward trend of the relative viscosity appears to be clear, though more work needs to be carried out to examine the upper limit that can be reached. Clearly, both porosity and shape (reflected in aspect ratio) of nanoparticles are critical factors for their role of enhancing viscosity.

Similarly, the larger amount of micropores included in WSC than RHC may be the reason that the WSC nanoparticles enhances viscosity better than RHC and nonporous metal oxide nanoparticles. However, the nanofluid of the more porous AC shows the striking viscosity enhancement.

#### 4. Conclusions

Two charcoals of wheat straw char (WSC) and rice husk char (RHC) as well as one active carbon (AC) were wet milled into their nanofluids in water. The charcoals and active carbon as well as their nanofluids were systematically characterised for their composition, surface chemistry, porosity, particle sizes, and particle interactions in the fluids at different pH values. The characterisation was then related to their viscosity increment with particle concentrations and pH values, and more importantly to the micropore structure. The Dispersion Factor analysis using the adapted Chen equation with the Dispersion Factor [22] shows that the WSC nanoparticles (with a size distribution peak located at 96 nm) has a DF value of 7.0, which is corresponding to a zeta-potential of -117 mV and strong interactions to the base liquid. The RHC nanoparticles (with a size distribution peak located at 154 nm) has a DF value of 4.5, corresponding to a zeta-potential of -115 mV. The DF values comprehensively reflect the effect of nanoparticle population (particle sizes) and interaction strength of the nanoparticle surface to the base liquid on the one hand and nanoparticle to nanoparticles interactions on the other hand in the fluid on the viscosity increment. The study shows that charcoal-based nanofluids give rise to better viscosity increments (DF = 7.0 for the WSC nanofluids) than that of metal oxide nanoparticles reported in the literature (DF = 6.6 for silica nanofluids) [22].

The AC nanoparticles show much more significant viscosity increment than the WSC and RHC nanoparticles, and the increment is comparable to that of carbon nanotubes at a concentration of < 0.6 vol%. As the nanoparticle concentration is higher than 0.6 vol%, the AC nanoparticles show continuously proportional viscosity enhancement following a linear equation for its 3D nano size. The proportional viscosity enhancement of the AC nanofluid is about 10 times higher than that of  $\gamma$ -alumina or titanium oxide nanoparticles. This study has shown that charcoal nanoparticles can provide better viscosity enhancement than metal oxide nanoparticles, and the viscosity enhancement can be adjusted by pH values. These properties and that the material is derived from bio-based waste sources that are available in massive quantities, as well as can now be valorised as viscosity enhancers favour charcoal-based nanofluids to be used as enhanced oil recovery fluids as our ongoing experimental work has demonstrated. The further development will provide a new route for carbon capture, utilisation, and sequestration.

#### CRedit authorship contribution statement

**Ifeoluwa Akande:** Writing – original draft. **Tony Bridgwater:** Supervision, Validation. **Petra J. van Koningsbruggen:** Validation. **Qingchun Yuan:** Conceptualization, Methodology, Supervision.

#### Declaration of Competing Interest

The authors declare that they have no known competing financial interests or personal relationships that could have appeared to influence the work reported in this paper.

#### Data availability

No data was used for the research described in the article.

#### Acknowledgement

The authors would like to thank Aston University for the start

funding provided to Dr Qingchun Yuan, thank Dr Jakub Sacharczuk for recording the ESEM images.

## References

- [1] IPCC, *Climate Change 2021: The Physical Science Basis. Contribution of Working Group I to the Sixth Assessment Report of the Intergovernmental Panel on Climate Change*. <https://www.ipcc.ch/report/ar6/wg1/#FullReport> Retrieved on 10 August. 2021.
- [2] Paris Agreement 2015. <https://unfccc.int/process-and-meetings/the-paris-agreement>. Retrieved on 07 July 2023.
- [3] CHANGE, U. N. F. C. O. C. Paris Agreement. 2015. United Nations Framework Convention on Climate Change.
- [4] BP 2020. Statistical Review of World Energy, 69<sup>th</sup> edition. <https://www.bp.com/content/dam/bp/business-sites/en/global/corporate/pdfs/energy-economics/statistical-review/bp-stats-review-2020-full-report.pdf>. Retrieved on 07 July 2023.
- [5] L. Hendraningrat, O. Torsæter, Metal oxide-based nanoparticles: revealing their potential to enhance oil recovery in different wettability systems, *Appl. Nanosci.* 5 (2015) 181–199.
- [6] A.E. Bayat, R. Junin, A. Samsuri, A. Piroozian, M. Hokmabadi, Impact of Metal Oxide Nanoparticles on Enhanced Oil Recovery from Limestone Media at Several Temperatures 28 (2014) 6255–6266.
- [7] N.A. Ogolo, O.A. Olafuyi, M.O. Onyekonwu, Enhanced Oil Recovery Using Nanoparticles. *SPE Saudi Arabia Section Technical Symposium and Exhibition*, Society of Petroleum Engineers, Al-Khobar, Saudi Arabia, 2012.
- [8] M.I. Youssif, R.M. El-Maghraby, S.M. Saleh, A. Elgibaly, Silica nanofluid flooding for enhanced oil recovery in sandstone rocks, *Egypt. J. Pet.* 27 (2018) 105–110.
- [9] S. Azarshin, J. Moghadasi, Z.A. Aboosadi, Surface functionalization of silica nanoparticles to improve the performance of water flooding in oil wet reservoirs, *Energy Exploration Exploitation* 35 (2017) 685–697.
- [10] T.X. Phuoc, M. Massoudi, R.-H. Chen, Viscosity and thermal conductivity of nanofluids containing multi-walled carbon nanotubes stabilized by chitosan, *Int. J. Therm. Sci.* 50 (2011) 12–18.
- [11] M.S. Alnarabiji, N. Yahya, A. Shafie, H. Solemani, K. Chandran, S.B.A. Hamid, K. Azizi, The Influence of Hydrophobic Multiwall Carbon Nanotubes Concentration on Enhanced Oil Recovery, *Procedia Eng.* 148 (2016) 1137–1140.
- [12] D. Battagazzore, S. Bocchini, J. Alongi, A. Frache, Rice husk as bio-source of silica: preparation and characterization of PLA–silica bio-composites, *RSC Adv.* 4 (2014) 54703–54712.
- [13] R. Sekifuji, M. Tatada, Study of the feasibility of a rice husk recycling scheme in Japan to produce silica fertilizer for rice plants, *Sustainable Environ. Res.* 29 (2019) 11.
- [14] X. Pan, Y. Sano, Acetic acid pulping of wheat straw under atmospheric pressure, *J. Wood Sci.* 45 (1999) 319–325.
- [15] F. Rego, H. Xiang, Y. Yang, J.L. Ordoñas, K. Chong, J. Wang, A. Bridgwater, Investigation of the role of feedstock properties and process conditions on the slow pyrolysis of biomass in a continuous auger reactor, *J. Anal. Appl. Pyrol.* 161 (2022), 105378.
- [16] W. Gondora, K. Doudin, D.J. Nowakowski, B. Xiao, Y. Ding, T. Bridgwater, Q. Yuan, Encapsulation of phase change materials using rice-husk-char, *Appl. Energy* 182 (2016) 274–281.
- [17] Y. Liu, X. Zhao, J. Li, D. Ma, R. Han, Characterization of bio-char from pyrolysis of wheat straw and its evaluation on methylene blue adsorption, *Desalin. Water Treat.* 46 (2012) 115–123.
- [18] E. Murozuka, T.C. de Bang, J. Frydenvang, J. Lindedam, K.H. Laursen, S. Bruun, J. Magid, J.K. Schjoerring, Concentration of mineral elements in wheat (*Triticum aestivum* L.) straw: Genotypic differences and consequences for enzymatic saccharification, *Biomass Bioenergy* 75 (2015) 134–141.
- [19] M.H.S. Abadi, A. Delbari, Z. Fakoor, J. Beadi, Effects of Annealing Temperature on Infrared Spectra of SiO<sub>2</sub> Extracted From Rice Husk 6 (2015) 41–45.
- [20] P. Innocenzi, Infrared spectroscopy of sol-gel derived silica-based films: a spectromicrostructure overview 316 (2003) 309–319.
- [21] C. Moore, T.S. Perova, B.J. Kennedy, K. Berwick, I.I. Shaganov, R.A. Moore, Study of structure and quality of different silicon oxides using FTIR and Raman microscopy 4876 (2003) 1247–1256.
- [22] I. Akande, T. Bridgwater, P.J. van Koningsbruggen, Q. Yuan, Advances in the modelling of concentration-dependent relative viscosity data for nanofluids by introducing the Dispersion Factor, *J. Mol. Liq.* 380 (2023), 121644.
- [23] H. Chen, W. Yang, Y. He, Y. Ding, L. Zhang, C. Tan, A.A. Lapkin, D.V. Bavykin, Heat transfer and flow behaviour of aqueous suspensions of titanatenanotubes (nanofluids), *Power Technology* 183 (2008) 63–72.
- [24] B.C. Pak, Y.I. Cho, Hydrodynamic and Heat Transfer Study of Dispersed Fluids with Submicron Metallic Oxide Particles, *Exp. Heat Transfer* 11 (1998) 151–170.
- [25] T.A. Saleh, V.K. Gupta, Chapter 4.5.3 Properties of Carbon Nanostructured, *Nanomaterial and Polymer Membranes - Synthesis, Characterization, and Applications*. Paperback ISBN: 9780128047033. Elsevier, 2016.
- [26] S. Abbasi, S.M. Zebarjad, S.H.N. Baghban, A. Youssefi, M.-S. Ekrami-Kakhki, Experimental investigation of the rheological behavior and viscosity of decorated multi-walled carbon nanotubes with TiO<sub>2</sub> nanoparticles/water nanofluids, *J. Therm. Anal. Calorim.* (2016).
- [27] I. Tavman, A. Turgut, M. Chirtoc, H.P. Schuchmann, S. Tavman, Experimental investigation of viscosity and thermal conductivity of suspensions containing nanosized ceramic particles, *Arch. Mater. Sci. Eng.* 34 (2) (2008) 99–104.